# Soluble Semiconductors AAsSe$_2$ (A = Li, Na) with a Direct-Band-Gap and Strong Second Harmonic Generation: A Combined Experimental and Theoretical Study

Tarun K. Bera,[†] Joon I. Jang,[‡] Jung-Hwan Song,[‡] Christos D. Malliakas,[†] Arthur J. Freeman,[‡] John B. Ketterson,[‡] and Mercouri G. Kanatzidis*,[†,§]

*Department of Chemistry and Department of Physics and Astronomy, Northwestern University, Evanston, Illinois 60208, and Materials Science Division, Argonne National Laboratory, Argonne, Illinois 60439*

Received November 21, 2009; E-mail: m-kanatzidis@northwestern.edu

**Abstract:** AAsSe$_2$ (A = Li, Na) have been identified as a new class of polar direct-band gap semiconductors. These I−V−VI$_2$ ternary alkali-metal chalcoarsenates have infinite single chains of $(1/\infty)[AsQ_2^-]$ derived from corner-sharing pyramidal AsQ$_3$ units with stereochemically active lone pairs of electrons on arsenic. The conformations and packing of the chains depend on the structure-directing alkali metals. This results in at least four different structural types for the Li$_{1-x}$Na$_x$AsSe$_2$ stoichoimetry ($\alpha$-LiAsSe$_2$, $\beta$-LiAsSe$_2$, $\gamma$-NaAsSe$_2$, and $\delta$-NaAsSe$_2$). Single-crystal X-ray diffraction studies showed an average cubic NaCl-type structure for $\alpha$-LiAsSe$_2$, which was further demonstrated to be locally distorted by pair distribution function (PDF) analysis. The $\beta$ and $\gamma$ forms have polar structures built of different $(1/\infty)[AsSe_2^-]$ chain conformations, whereas the $\delta$ form has nonpolar packing. A wide range of direct band gaps are observed, depending on composition: namely, 1.11 eV for $\alpha$-LiAsSe$_2$, 1.60 eV for LiAsS$_2$, 1.75 eV for $\gamma$-NaAsSe$_2$, 2.23 eV for NaAsS$_2$. The AAsQ$_2$ materials are soluble in common solvents such as methanol, which makes them promising candidates for solution processing. Band structure calculations performed with the highly precise screened-exchange sX-LDA FLAPW method confirm the direct-gap nature and agree well with experiment. The polar $\gamma$-NaAsSe$_2$ shows very large nonlinear optical (NLO) second harmonic generation (SHG) response in the wavelength range of 600−950 nm. The theoretical studies confirm the experimental results and show that $\gamma$-NaAsSe$_2$ has the highest static SHG coefficient known to date, 337.9 pm/V, among materials with band gaps larger than 1.0 eV.

## 1. Introduction

Coherent and tunable sources of mid-infrared (mid-IR) radiation are useful in a wide range of scientific and technological applications ranging from spectroscopy and frequency metrology to information technology, industrial process control, photochemistry, explosives detection, and photomedicine.[1] Acentric inorganic compounds are the basis for nonlinear (NLO) materials generating coherent radiation extending from the ultraviolet (UV) to the far-IR.[2] Boron oxide materials, e.g., LiB$_3$O$_5$ (LBO), $\beta$-BaB$_2$O$_4$ (BBO), etc., have proven superior in

the UV to near-visible region,[3] whereas in the visible region, metal oxides, e.g., KTiOPO$_4$ (KTP), LiNbO$_3$ (LN), etc., are used. In the mid-IR to the far-IR region, metal oxides suffer from lower efficiencies and optical transparency, which arise from the absorption bands of metal−oxygen bonds and their overtones.[4] Polar chalcogenide semiconductors can be more transparent in this region, but only a few, e.g., AgGaSe$_2$, AgGaS$_2$, and GaSe, possess the necessary attributes for second harmonic generation (SHG) applications: i.e., good SHG susceptibility, large birefringence, good optical transparency, acceptable laser damage threshold, chemical stability, etc.[2,5] Therefore, materials that are active in the IR region are of broad interest.

In SHG, doubling of a given fundamental frequency is accomplished by the nonlinear response of the material. The presence of strong dipoles and polarizable atoms in the system can give rise to intense SHG response if the packing of

[†] Department of Chemistry, Northwestern University.
[‡] Department of Physics and Astronomy, Northwestern University.
[§] Argonne National Laboratory.

(1) (a) Schunemann, P. G. *Proc. SPIE-Int. Soc. Opt. Eng.* **2007**, *6455*, 64550R–1. (b) Bordui, P. F.; Fejer, M. M. *Annu. Rev. Mater. Sci.* **1993**, *23*, 321–379. (c) Ebrahim-Zadeh, M.; Sorokina, I. T. *Mid-Infrared Coherent Sources and Applications*; NATO Science for Peace and Security Series B: Physics and Biophysics; Springer: New York, 2007. (d) Hazama, H.; Takatani, Y.; Awazu, K. *Proc. SPIE-Int. Soc. Opt. Eng.* **2007**, *6455*, 645507–1.

(2) (a) Nikogosyan, D. N. *Nonlinear Optical Crystals: A Complete Survey*; Springer: New York, 2005. (b) Liao, J. H.; Marking, G. M.; Hsu, K. F.; Matsushita, Y.; Ewbank, M. D.; Borwick, R.; Cunningham, P.; Rosker, M. J.; Kanatzidis, M. G. *J. Am. Chem. Soc.* **2003**, *125*, 9484–9493. (c) Baudrier-Raybaut, M.; Haidar, R.; Kupecek, P.; Lemasson, P.; Rosencher, E. *Nature* **2004**, *432*, 374–376. (d) Chen, C.; Ye, N.; Lin, J.; Jiang, J.; Zeng, W.; Wu, B. *Adv. Mater.* **1999**, *11*, 1071.

(3) (a) Sasaki, T.; Mori, Y.; Yoshimura, M.; Yap, Y. K.; Kamimura, T. *Mater. Sci. Eng.* **2000**, *30*, 1–54. (b) Chen, C.; Lin, Z.; Wang, Z. *Appl. Phys. B* **2005**, *80*, 1–25.

(4) (a) Fossier, S. *J. Opt. Soc. Am. B* **2004**, *21*, 1981. (b) Panyutin, V.; Badikov, V.; Shevyrdyaeva, G.; Mitin, K.; Seryogin, A.; Petrov, V.; Noack, F. *Proc. SPIE-Int. Soc. Opt. Eng.* **2008**, *6875*, 68750A–1. (c) Bhar, G. C. *Jpn. J. Appl. Phys.* **1993**, *32*, 653–659.

(5) Goodman, C. H. L. *Semicond. Sci. Technol.* **1991**, *6*, 725.

asymmetric building units is noncentrosymmetric.[6] Numerous strategies have been suggested to discover better SHG materials, but the rational design of such materials remains a challenge. Materials design exploiting asymmetric building units in the oxides includes Jahn–Teller distorted $d^0$ metal centers (e.g., $Ti^{4+}$, $Nb^{5+}$, $Mo^{6+}$, etc.),[7] anionic groups with stereochemically active lone pairs (e.g., $[IO_3]^-$, $[TeO_x]^{n-}$, etc.),[8] and noncentrosymmetric $\pi$-orbital systems (e.g., $[BO_3]^{3-}$ and $[B_3O_6]^{3-}$).[9] Corresponding units in the chalcogenides such as the trigonal-pyramidal building anions (e.g., $[AsSe_3]^{3-}$, $[SbS_3]^{3-}$, $[TeS_3]^{2-}$ etc.) have been little explored.[6a,10]

The $AAsQ_2$ (A = alkali metal; Q = S, Se) chalcoarsenates are part of the I−V−VI$_2$ family and have the pyramidal asymmetric unit $[AsQ_3]^{3-}$.[11] Corner sharing of $[AsQ_3]^{3-}$ pyramids leads to infinite $(1/\infty)[AsQ_2^-]$ polymeric chains adopting different conformations.[12,13] The conformation of a single chain depends on the counterions: e.g., $KAsSe_2$ and $RbAsSe_2$ exhibit *vierer* and $CsAsSe_2$ *zweier* single chains, respectively. Crystal structures for some of these compounds have been studied, but generally these materials have not been examined in detail in terms of their physical properties.[14]

Recently, we described the $AAsS_2$ (A = Li, Na[12a]) compounds,[15] where the Li and Na analogues have polar and nonpolar crystal structures, respectively. The SHG response of $LiAsS_2$ was reported to be 10-fold relative to that of the commercial material $AgGaSe_2$, and it increases with Na substitution in the $Li_{0.6}Na_{0.4}AsS_2$ to approach $\sim 30\times$ greater than that of $AgGaSe_2$.

Here we extended our investigations of the alkali-metal chalcoarsenate (AAsQ) systems to the selenide systems. As selenium is more polarizable than sulfur, we expected an even greater SHG response. In the process of these studies we discovered a new polar direct band gap material, namely $\beta$-LiAsSe$_2$ and the 80% Na substituted $\beta$-Li$_{0.2}$Na$_{0.8}$AsSe$_2$, with an SHG response $\sim 60$ times greater than that of $AgGaSe_2$. The compound $\beta$-Li$_{0.2}$Na$_{0.8}$AsSe$_2$ was found to have the noncen-

trosymmetric polymorph $\gamma$-Li$_{0.2}$Na$_{0.8}$AsSe$_2$, which has a new $(1/\infty)[AsSe_2^-]$ chain conformation. The Na substitution in $\gamma$-Li$_{0.2}$Na$_{0.8}$AsSe$_2$ proceeds to 100% while preserving the polar structure, resulting in $\gamma$-NaAsSe$_2$, which also exhibits a remarkably high SHG response. The $\delta$-NaAsSe$_2$ is a centrosymmetric analogue with a different $(1/\infty)[AsSe_2^-]$ chain conformation. These results propel the $AAsSe_2$ materials to the top category of NLO-SHG systems possessing among the highest responses ever reported.

For the first time, a theoretical approach was applied to these materials, where band structure analysis derived from the first-principles calculations was used to calculate the SHG susceptibility coefficients. The theoretical studies confirm the experimental results and show that $\gamma$-NaAsSe$_2$ has the highest static SHG coefficient known to date, 337.9 pm/V, among materials with band gaps larger than 1.0 eV. First-principles total energy calculations were also used to explain the physical origin behind the thermodynamic stability of $\gamma$-NaAsSe$_2$ relative to $\delta$-NaAsSe$_2$.[13a] Finally, using pair distribution function (PDF) analysis, we show that the local structure of cubic $\alpha$-LiAsSe$_2$ deviates significantly from the NaCl-type structure suggested from single-crystal X-ray analysis.

## 2. Experimental Section

**2.1. Reagents.** The chemicals in this work were used as obtained: (i) sulfur powder, sublimed, 99.5%, 100 mesh, Alfa Aesar; (ii) lithium metal rods, 99.9%, 12.7 mm diameter, Aldrich Chemical Co.; (iii) sodium metal cubes, 99.95%, Aldrich Chemical Co.; (iv) As, 99.9%, Aldrich Chemical Co.; (v) *N,N*-dimethylformamide (Spectrum Chemicals, ACS reagent grade); (vi) diethyl ether (Columbus Chemical Industries, Columbus, WI, ACS reagent grade, anhydrous). (vii) Se (99.9999%, 5NPlus, Quebec, Canada).

**2.2. Synthesis.** All manipulations were carried out under a dry nitrogen atmosphere in a Vacuum Atmospheres Dri-lab glovebox. $A_2S$ and $A_2Se$ (A = Li, Na) starting materials were prepared by a modified literature procedure by reacting stoichiometric amounts of the elements in liquid ammonia.[16]

**2.2.1. Synthesis of $\alpha$-LiAsSe$_2$ (I).** An 0.056 g (0.60 mmol) amount of Li$_2$Se, 0.090 g (1.20 mmol) of As, and 0.143 g (1.80 mmol) of Se were loaded into a fused-silica tube. The tube was flame-sealed under vacuum ($\sim 5 \times 10^{-4}$ mbar) and inserted into a programmable furnace. The temperature was increased from 50 to 500 °C in 5 h. It was held there for 2 h followed by quenching in water. The phase-pure black crystalline product ($\sim 98\%$ yield) was isolated by carefully breaking the tube. Semiquantitative energy dispersive spectroscopic (EDS) analysis using a scanning electron microscope (SEM) on a number of different crystals indicated the presence of both As and Se (As:Se $\approx$ 1:2).

**2.2.2. Synthesis of $\beta$-LiAsSe$_2$ (II). 2.2.2.1. Method 1.** An 0.056 g (0.60 mmol) amount of Li$_2$Se, 0.090 g (1.20 mmol) of As, and 0.143 g (1.80 mmol) of Se were loaded into a fused-silica tube. The tube was flame-sealed under vacuum ($\sim 5 \times 10^{-4}$ mbar) and inserted into a programmable furnace. The temperature was increased from 50 to 500 °C in 5 h. It was held there for 10 h and then cooled at a rate of 10 °C/h to 250 °C followed by cooling in air. A phase-pure black crystalline product was isolated in $\sim 96\%$ yield. Semiquantitative energy dispersive spectroscopic (EDS) analysis using a scanning electron microscope (SEM) on a number of different crystals indicated the presence of both As and Se (As: Se $\approx$ 1:2).

(6) (a) Ye, N.; Chen, Q.; Wu, B.; Chen, C. *J. Appl. Phys.* **1998**, *84*, 555. (b) Bergman, J. G. J.; Boyd, G. D.; Ashkin, A.; Kurtz, S. K. *J. Appl. Phys.* **1969**, *40*, 2860.

(7) (a) Halasyamani, P. S. *Chem. Mater.* **2004**, *16*, 3586. (b) Muller, E. A.; Cannon, R. J.; Sarjeant, A. N.; Ok, K. M.; Halasyamani, P. S.; Norquist, A. J. *Cryst. Growth Des.* **2005**, *5*, 1913.

(8) (a) Phanon, D.; Gautier-Luneau, I. *Angew. Chem., Int. Ed.* **2007**, *46*, 8488. (b) Chi, E. O.; Ok, K. M.; Porter, Y.; Halasyamani, P. S. *Chem. Mater.* **2006**, *18*, 2070.

(9) (a) Pan, S.; Smit, J. P.; Watkins, B.; Marvel, M. R.; Stern, C. L.; Poeppelmeier, K. R. *J. Am. Chem. Soc.* **2006**, *128*, 11631. (b) Chen, C.; Wang, Y.; Wu, B.; Wu, K.; Zeng, W.; Yu, L. *Nature* **1995**, *373*, 322–324.

(10) (a) Distanov, V. E.; Nenashev, B. G.; Kirdyashkin, A. G.; Serboulenko, M. G. *J. Cryst. Growth* **2002**, *235*, 457–464. (b) Feichtner, J. D.; Roland, G. W. *Appl. Opt.* **1972**, *11*, 993. (c) Zhang, X.; Kanatzidis, M. G. *J. Am. Chem. Soc.* **1994**, *116*, 1890.

(11) (a) Sheldrick, W. S.; Wachhold, M. *Coord. Chem. Rev.* **1998**, *176*, 211–322. (b) Drake, G. W.; Kolis, J. W. *Coord. Chem. Rev.* **1994**, *137*, 131–178. (c) Dehnen, S.; Melullis, M. *Coord. Chem. Rev.* **2007**, *251*, 1259–1280.

(12) (a) Palazzi, M.; Jaulmes, S. *Acta Crystallogr., Sect. B* **1977**, *33*, 908. (b) Yang, Z. M.; Pertlik, F. *J. Alloys Compd.* **1994**, *216*, 155–158.

(13) (a) Eisenmann, B.; Schafer, H. *Z. Anorg. Allg. Chem.* **1979**, *456*, 87–94. (b) Sheldrick, W. S.; Hausler, H. J. *Z. Anorg. Allg. Chem.* **1988**, *561*, 139–148.

(14) (a) Dovgoshe, N.; Nikolyuk, V. I.; Semrad, E. E.; Chepur, D. V.; Golovei, M. I. *Izv. Vyssh. Uchebn. Zaved., Fiz.* **1970**, *13*, 138–9. (b) Lada, A. V.; Zuban, V. A.; Borets, A. N.; Golovei, M. I. *Opt. Spektrosk.* **1974**, *37*, 582–586. (c) Bazakutsa, V. A.; Gnidash, N. I.; Perekrestov, V. I.; Lazarev, V. B.; Salov, A. V.; Trippel, A. F. *Inorg. Mater.* **1987**, *23*, 1020–1023.

(15) Bera, T. K.; Song, J. H.; Freeman, A. J.; Jang, J. I.; Ketterson, J. B.; Kanatzidis, M. G. *Angew. Chem., Int. Ed.* **2008**, *120*, 7946.

(16) (a) Feher, F. In *Handbuch der Praeparativen Anorganischen Chemie*; Brauer, G., Ed.; Ferdinand Enke: Stuttgart, Germany, 1954; Vol. 1, pp 280−281. (b) Aitken, J. A.; Chondroudis, K.; Young, V. G.; Kanatzidis, M. G. *Inorg. Chem.* **2000**, *39*, 1525–1533. (c) Kanatzidis, M. G.; Sutorik, A. C. *Prog. Inorg. Chem.* **1995**, *43*, 151.

**2.2.2.2. Method 2 (Flame Reaction).** If large single crystals are not necessary, the following preparation can be used. The flame-sealed tube from method 1 was melted over a flame until the whole mixture became a black melt. It was then air-cooled to produce a pure black microcrystalline product ($\sim$94% yield). Powder X-ray diffraction gave the same pattern as observed using method 1. Methods 1 and 2 can both be used to synthesize phase-pure $\beta$-$Li_{1-x}Na_{-x}AsSe_2$ solid solutions in the composition range $0 \leq x \leq 0.5$ using respective stoichiometric mixtures of starting materials.

**2.2.3. Synthesis of $\beta$-$Li_{0.2}Na_{0.8}AsSe_2$ (IIa).** An 0.011 g (0.12 mmol) amount of $Li_2Se$, 0.059 g (0.47 mmol) of $Na_2Se$, 0.088 g (1.17 mmol) of As, and 0.140 g (1.76 mmol) of Se were loaded into a fused-silica tube. The tube was flame-sealed under vacuum ($\sim$5 $\times$ 10$^{-4}$ mbar) and melted over a flame until the whole mixture became a black melt. It was then quenched in water, and phase-pure black microcrystalline product ($\sim$98% yield) was obtained. Semiquantitative energy dispersive spectroscopic (EDS) analysis using a scanning electron microscope (SEM) on a number of crystals gave an average composition of $Na_{0.7}As_{1.1}Se_{2.2}$. The powder X-ray diffraction pattern was similar to that of **II**, except peaks shifted to lower $2\theta$ by a few degrees. Quenching the reaction in air produces a mixture of $\beta$- and $\gamma$-$Li_{0.2}Na_{0.8}AsSe_2$.

**2.2.4. Synthesis of $\gamma$-$Li_{0.2}Na_{0.8}AsSe_2$ (IIIa).** An 0.011 g (0.12 mmol) amount of $Li_2Se$, 0.059 g (0.47 mmol) of $Na_2Se$, 0.088 g (1.17 mmol) of As, and 0.140 g (1.76 mmol) of Se were loaded into a fused-silica tube. The tube was flame-sealed under vacuum ($\sim$5 $\times$ 10$^{-4}$ mbar) and inserted into a programmable furnace. The temperature was increased from 50 to 500 °C over 5 h. It was held there for 10 h and then cooled at a rate of 10 °C/h to 250 °C followed by cooling in air. Phase-pure black crystalline product ($\sim$93% yield) was obtained. Semiquantitative energy dispersive spectroscopic (EDS) analysis using a scanning electron microscope (SEM) on a number of crystals gave an average composition of $Na_{0.7}As_{1.1}Se_{2.2}$. The $\gamma$-$NaAsSe_2$ (**III**) was prepared from a mixture of 0.084 g (0.67 mmol) of $Na_2Se$, 0.100 g (1.33 mmol) of As and 0.158 g (1.99 mmol) of Se using a procedure similar to the synthesis of **IIIa**.

**2.2.5. Synthesis of $\delta$-$NaAsSe_2$ (IV).** An 0.084 g (0.67 mmol) amount of $Na_2Se$, 0.100 g (1.33 mmol) of As, and 0.158 g (2.00 mmol) of Se were loaded into a fused-silica tube. The tube was flame-sealed under vacuum ($\sim$5 $\times$ 10$^{-4}$ mbar) and melted over a flame until the whole mixture became a black melt. It was then quenched in water or in air to give pure black microcrystalline product in $\sim$98% yield. Semiquantitative energy dispersive spectroscopic (EDS) analysis using a scanning electron microscope (SEM) on a number of crystals gave an average composition of $Na_{1.1}As_{1.0}Se_{2.2}$. The powder X-ray diffraction pattern was similar to the previously reported one.[13a]

**2.3. Physical Measurements. 2.3.1. Powder X-ray Diffraction Analysis.** Powder X-ray diffraction analyses were performed using a calibrated (against NIST silicon) CPS 120 INEL X-ray powder diffractometer (Cu K$\alpha$ graphite-monochromated radiation) operating at 40 kV/20 mA and equipped with a position-sensitive detector with flat sample geometry. Theoretical powder diffraction patterns from single-crystal X-ray data were calculated using the PowderCell, v 2.3 software package.[17]

**2.3.2. Electron Microscopy.** Semiquantitative microprobe analyses of the compounds were performed with a Hitachi S-3400 scanning electron microscope (SEM) equipped with a PGT energy dispersive X-ray analyzer. Data were acquired with an accelerating voltage of 25 kV and a 60 s accumulation time.

**2.3.3. Solid-State UV/Vis/Near-IR Spectroscopy.** Optical diffuse reflectance measurements were performed at room temperature using a Shimadzu UV-3101PC double-beam, double-monochromator spectrophotometer. The instrument is equipped with an integrating sphere detector and controlled by a computer. $BaSO_4$ was used as a 100% reflectance standard. The samples were

prepared by grinding the crystals to a powder and spreading it on a compacted surface of the powdered standard material, preloaded into a sample holder. The reflectance versus wavelength data generated were used to estimate the band gap of the materials by converting reflectance to absorption data using the Kubelka−Munk equation.[18]

**2.3.4. Raman Spectroscopy.** Raman spectra were recorded on a BIORAD FT-Raman II spectrograph equipped with a Nd:YAG infrared continuous wave laser ($\lambda = 1064$ nm) and a liquid nitrogen cooled germanium detector. A finely powdered sample in a Pyrex capillary tube was used for the spectral study after calibrating the spectrometer with KBr. Laser power at the sample was estimated to be about 5 mW, and the focused laser beam diameter was ca. 10 $\mu$m. A total of 20 scans were sufficient to obtain good-quality spectra.

**2.3.5. Differential Thermal Analysis (DTA).** Thermal analysis was performed on a Shimadzu DTA-50 thermal analyzer. Typically a sample ($\sim$30 mg) of ground crystalline material was sealed in a silica ampule under vacuum. A similar ampule of equal mass filled with $Al_2O_3$ was sealed and placed on the reference side of the detector. The sample was heated to 600 °C at 10 °C/min and, after 1 min, was cooled at a rate of −10 °C/min to 50 °C. The residues of the DTA experiments were examined by X-ray powder diffraction. The reproducibility of the results was confirmed by running multiple heating/cooling cycles. The melting and crystallization points were measured at the minimum of the endothermic peak and at the maximum of the exothermic peak, respectively.

**2.3.6. X-ray Crystallography.** The crystal structure was determined by single-crystal X-ray diffraction methods. Rectangular needlelike crystals were chosen for the single-crystal X-ray diffraction study. Data collections were done at 100 K using a STOE imaging plate diffraction system (IPDS-II) with graphite-monochromated Mo K$\alpha$ radiation operating at 50 kV and 40 mA with a 34 cm image plate. Individual frames were collected with scan widths of 1.0° in $\omega$ and 5 min exposure time. The X-AREA, X-RED, and X-SHAPE software packages were used for data extraction and integration and to apply analytical absorption corrections.[19a] Direct methods and full-matrix least-squares refinement against $F^2$ were performed with the SHELXTL package.[19b] For **IIa** and **IIIa,** both Na and Li atoms were constrained to a common site using the EXYZ command along with the EADP command to constrain the thermal parameters for Li and Na sites. $\gamma$-$NaAsSe_2$ was found to have only a 0.5% racemic twin (100, 010, 001). The parameters for data collection and the details of the structural refinements are given in Table 1. Fractional atomic coordinates and displacement parameters for each structure are given in the Supporting Information.

**2.3.7. Pair Distribution Function (PDF) Analysis.** Both powder samples ($\alpha$-$LiAsSe_2$ and $\beta$-$LiAsSe_2$) were packed in Kapton capillaries (1 mm diameter), and diffraction data were collected at 100 K using the rapid acquisition pair distribution function (RA-PDF) technique.[20a] Data were collected using an MAR345 image plate detector and 87 keV energy X-rays ($\lambda = 0.142\,411$ Å) at the 6-IDD beamline at the APS. Measurements were taken for 30−90 s (depending on the scattering properties of each sample) and repeated around six times to improve counting statistics. The data were combined and integrated using the program FIT2D.[20b] Various corrections were made to the data, such as subtraction of background and container, Compton and fluorescence scattering, geometric corrections, absorption, etc.[20c] Corrections were made using the program PDFgetX2.[20d] Finally, $S(Q)$ was truncated at a $Q_{max}$ value

(17) Kraus, W.; Nolze, G. PowderCell 2.3, 1998.

(18) (a) Pankove, J. I. In *Optical Processes in Semiconductors*; Dover Publications: New York, 1975.

(19) (a) X-Area, Version 1.39; STOE & Cie GmbH, Darmstadt. Germany, 2006. (b) SHELXTL, Version 5.03; Siemens Analytical X-ray Instruments, Madison, WI, 1995.

**Table 1.** Crystallographic Refinement Details for α-LiAsSe$_2$, β-LiAsSe$_2$, and γ-NaAsSe$_2$

|  | α-LiAsSe$_2$ | β-LiAsSe$_2$ | γ-NaAsSe$_2$ |
|---|---|---|---|
| wavelength, Å | 0.710 73 | 0.710 73 | 0.710 73 |
| cryst syst | cubic | monoclinic | monoclinic |
| space group | $Fm\bar{3}m$ | $Cc$ | $Pc$ |
| unit cell dimens |  |  |  |
| $a$, Å | 5.5573(6) | 12.2872(14) | 11.682(2) |
| $b$, Å |  | 5.5419(7) | 5.9021(12) |
| $c$, Å |  | 5.5533(6) | 11.823(2) |
| $\beta$, deg |  | 113.12(8) | 90.45(3) |
| $V$, Å$^3$ | 171.63(3) | 347.79(7) | 815.2(3) |
| $Z$ | 2 | 4 | 2 |
| temp, K | 100 | 100 | 100 |
| calcd density, g/cm$^3$ | 4.640 | 4.579 | 4.169 |
| abs coeff, mm$^{-1}$ | 30.183 | 30.412 | 26.062 |
| $F(000)$ | 208 | 416 | 896 |
| $\theta$ range for data collecn, deg | 6.36−28.59 | 3.61−29.13 | 3.45−29.18 |
| no. of rflns collected | 391 | 1560 | 5842 |
| no. of indep rflns | 23 | 845 | 3339 |
| refinement method | full-matrix least squares on $F^2$ |  |  |
| completeness to $\theta$, % | 100 | 99.8 | 95.1 |
| $R$(int), % | 4.38 | 2.60 | 6.33 |
| no. of params | 4 | 38 | 147 |
| goodness of fit on $F^2$ | 1.383 | 1.142 | 1.126 |
| final $R$ indices [$I > 2\sigma(I)$]: R1$^a$/wR2$^b$ (%) | 3.53/8.40 | 2.43/4.82 | 4.98/11.65 |
| $R$ indices (all data): R1$^a$/wR2$^b$ (%) | 3.53/8.40 | 2.92/4.92 | 6.50/13.59 |
| largest diff peak/hole, e Å$^{-3}$ | 1.170/−0.947 | 0.880/−0.923 | 1.681/−1.860 |

$^a$ R1 = $\sum||F_o| - |F_c||/\sum|$. $^b$ wR2 = $\{\sum w(F_o^2 - F_c^2)^2/\sum w(F_o^2)^2\}^{1/2}$.

of 24 Å$^{-1}$ before the PDF was calculated. Simulations were carried out using PDFfit2.[20e]

**2.3.8. Nonlinear Optical Property Measurements.** Powder SHG measurements on polycrystalline samples were performed on a modified Kurtz-NLO system.[21] A frequency-tripled output of a passive-active mode-locked Nd:YAG laser with a pulse width of about 15 ps and a repetition rate of 10 Hz to pump an optical parametric amplifier (OPA) was used as a 1580 nm laser source. The OPA generates vertically polarized pulses in the ranges 400−685 and 737−3156 nm. In this range, the spectral bandwidth of the linearly polarized light from the OPA was rather broad, about 2 meV full width at half-maximum. However, the phase space compression phenomena ensures effective SHG, since lower energy portions were exactly compensated for by higher parts, thereby satisfying both energy and momentum conservation. Because the SHG efficiency has been shown to depend strongly on particle size, polycrystalline samples were ground and sieved into distinct particle size ranges. To make relevant comparisons with the benchmark SHG material, crystalline AgGaSe$_2$[22] was also ground and sieved into the same particle size ranges. Powders with particle sizes of 45−63 $\mu$m were used for comparing SHG intensities. Sieved powder samples of the specified particle size were placed in capillary tubes. An incident laser pulse of 80 $\mu$J was focused onto

a spot 500 $\mu$m in diameter using a 3 cm focal-length lens, and the SHG signal was collected in reflection geometry from the excitation surface and focused onto a fiber optic bundle. The output of the fiber optic bundle was coupled to the entrance slit of a Spex Spec-One 500 M spectrometer and detected using a nitrogen-cooled CCD camera. The data collection time was 60 s for both samples and the reference material (AgGaSe$_2$). Since the SHG process is a second-order process, the measured SHG intensity is proportional to the square of the laser pulse energy. Measured intensity data points were normalized by dividing by the square of the laser pulse energy. This scaling directly corresponds to the SHG intensity when we use a 1 $\mu$J pulse.

**2.4. Band Structure and Total Energy Calculations.** This was done using the full-potential linearized augmented plane wave (FLAPW)[23a] method with the screened-exchange local density approximation (sX-LDA)[23b] as well as the Hedin−Lundqvist form of the exchange-correlation potential (LDA).[23c] The core states and the valence states were treated fully relativistically and scalar relativistically, respectively. We employed the experimental lattice parameters and atomic coordinates. The energy cutoffs for the interstitial plane-wave basis and the star functions were 13.0 and 144.0 Ry, respectively.

## 3. Results and Discussion

**3.1. Crystal Structure. 3.1.1. Structure of α-LiAsSe$_2$ (I).** The structure of **I** is cubic NaCl type and is similar to that observed in the heavier M elements (e.g., Sb, Bi) of NaMQ$_2$.[24] A view of the unit cell is shown in Figure 1a. Both As and Li occupy a single cationic site (50% occupancy) with a distance of 2.7787(3) Å from Se (see Tables 1 and 2 for crystallographic refinement and bond distance details, respectively). As we will show below using the PDF technique,[25] the NaCl-type structure of **I** is only an artifact that results from the averaging of a NaCl-type cubic unit cell. We will show that the structure is in fact locally heavily disordered.

**3.1.2. Structure of β-LiAsSe$_2$ (II).** This form crystallizes in the noncentrosymmetric space group $Cc$ and is isostructural with LiAsS$_2$. It consists of densely packed $(1/\infty)$[AsSe$_2^-$] polymeric chains and alkali-metal ions. The alignment of the chains parallel to the $c$ axis is shown in Figure 1b. The AsSe$_3$ pyramid provides the molecular building units in the $(1/\infty)$[AsSe$_2^-$] chains via corner bridging. Analogous chains are also present as *zweier* single chains (Figure 2a) in NaAsS$_2$ and δ-NaAsSe$_2$, where the packing of chains is centrosymmetric (Figure 1e).[13a] The As−Se and Li−Se distances are normal[26] (Table 2). The alkali-metal ions are in a distorted-octahedral environment of Se atoms, and the ASe$_6$ octahedron forms a three-dimensional network by itself through edge sharing in the $bc$ plane and corner sharing along the $a$ direction (see the Supporting Information).

Each AsSe$_3$ trigonal pyramid in the chain has two different Se atoms: terminal $\mu_1$-Se and bridging $\mu_2$-Se atoms. The terminal Se atom forms strong 4p(Se) to 4p(As) back $\pi$-bonding, resulting in shorter As−Se bond distances (~2.327 Å) compared

(20) (a) Chupas, P. J.; Qiu, X.; Hanson, J. C.; Lee, P. L.; Grey, C. P.; Billinge, S. J. L. *J. Appl. Crystallogr.* **2003**, *36*, 1342–1347. (b) Hammersley, A. P.; Svensson, S. O.; Hanfland, M.; Fitch, A. N.; Hausermann, D. *High Pressure Res.* **1996**, *14*, 235–248. (c) Egami, T.; Billinge, S. J. L. *Underneath the Bragg Peaks: Structural Analysis of Complex Materials*; Pergamon Press: Amsterdam, 2003. (d) Qiu, X.; Thompson, J. W.; Billinge, S. J. L. *J. Appl. Crystallogr.* **2004**, *37*, 678. (e) Farrow, C. L.; Juhas, P.; Liu, J. W.; Bryndin, D.; Bozin, E. S.; Bloch, J.; Proffen, T.; Billinge, S. J. L. *J. Phys. Cond. Matter* **2007**, *19*, 335219/1–335219/7.

(21) (a) Kurtz, S. K.; Perry, T. T. *J. Appl. Phys.* **1968**, *39*, 3798. (b) Ok, K. M.; Chi, E. O.; Halasyamani, P. S. *Chem. Soc. Rev.* **2006**, *35*, 710.

(22) Kanellis, G.; Kambas, C.; Spyridelis, J. *Mater. Res. Bull.* **1976**, *11*, 429–436.

(23) (a) Wimmer, E.; Krakauer, H.; Weinert, M.; Freeman, A. J. *Phys. Rev. B* **1981**, *24*, 864. (b) Bylander, D. M.; Kleinman, L. *Phys. Rev. B* **1990**, *41*, 7868. (c) Hedin, L.; Lundqvis, B. I. *J. Phys. C* **1971**, *4*, 2064.

(24) Olivier-Fourcade, P. J.; Philippot, E.; Maurin, M. *Z. Anorg. Allg. Chem.* **1978**, *446*, 159–168.

(25) (a) Billinge, S. J. L.; Kanatzidis, M. G. *Chem. Commun.* **2004**, *7*, 749–760. (b) Warren, B. E., *X-ray Diffraction*; Dover Publications: New York, 1990.

(26) (a) Iyer, R. G.; Do, J.; Kanatzidis, M. G. *Inorg. Chem.* **2003**, *42*, 1475. (b) Wachhold, M.; Kanatzidis, M. G. *Inorg. Chem.* **2000**, *39*, 2337–2343. (c) Do, J.; Kanatzidis, M. G. *J. Alloys Compd.* **2004**, *381*, 41–49.
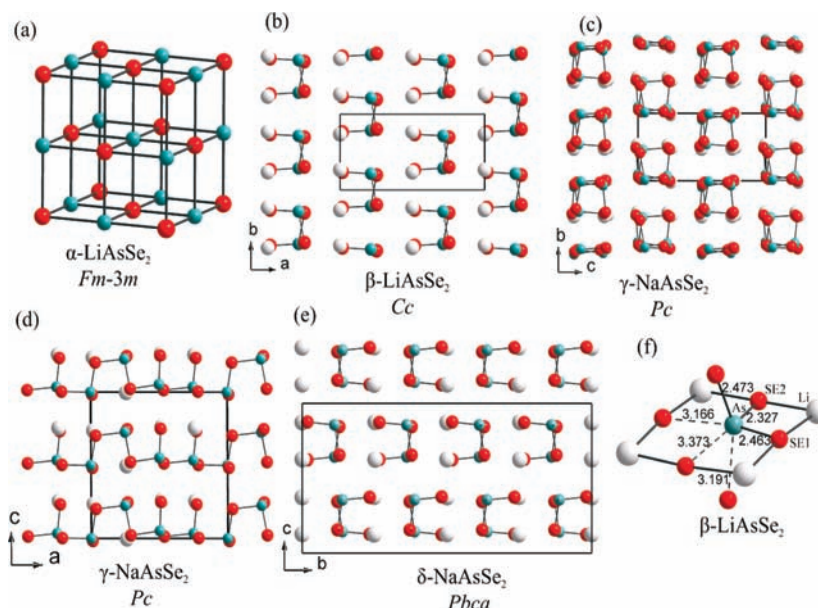
**Figure 1.** Extended unit cell view of four polymorphs of $Li_{1-x}Na_xAsSe_2$: (a) NaCl-type packing of Li/As (blue) and Se (red) in the α form; (b) noncentrosymmetric alignment of the *zweier* single chains $(1/\infty)[AsSe_2^-]$ in the β form (view down the *c* axis); (c) packing of the *vierer* single chains $(1/\infty)[AsSe_2^-]$ in the γ form (view down the *a* axis); (d) corresponding view down the *b* axis; (e) view down the *a* axis of the δ-NaAsSe$_2$ structure, with the centrosymmetric alignment of the *zweier* single chains $(1/\infty)[AsSe_2^-]$ clearly evident; (f) coordination environment of As in β-LiAsSe$_2$, showing three strong As−S interactions (solid line) and three weak interactions (dashed line). All forms are ordered variants of the archetype NaCl structure.

**Table 2.** Selected Bond Distances (Å) and Angles (deg) for α-LiAsSe$_2$ and β-LiAsSe$_2$ at 100 K with Standard Deviations in Parentheses

| α-LiAsSe$_2$ | | | |
|---|---|---|---|
| As/Li−Se | | 2.7787(3) | |
| As/Li−Se−As/Li | | 90.0 | |

| β-LiAsSe$_2$ | | | |
|---|---|---|---|
| As−Se(2) | 2.3266(11) | Li−Se(1) | 2.902(16) |
| As−Se(1) | 2.4635(10) | Li−Se(2) | 2.763(19) |
| As−Se(1) | 2.4728(10) | Li−Se(2) | 2.68(2) |
| Se(2)−As−Se(1) | 103.53(4) | Li−Se(1) | 2.772(16) |
| Se(2)−As−Se(1) | 102.72(5) | Li−Se(2) | 2.796(19) |
| Se(1)−As−Se(1) | 96.04(5) | Li−Se(2) | 2.87(2) |

to the bridging As−Se distances (∼2.473 Å). The presence of two different As−Se bonds was also confirmed by Raman spectroscopy (Figure 3). The high-energy peak in the range of $270-290$ cm$^{-1}$ can be assigned to the As−Se$_{terminal}$ stretching mode, the medium-energy peaks in the range of $180-210$ cm$^{-1}$ can be assigned to the As−Se$_{bridging}$ stretching modes, and the low-energy peaks in the range of $70-150$ cm$^{-1}$ can be assigned to the Se−As−Se bending modes.[27] There is a blue shift of the Raman peaks with increasing Na substitution in β-Li$_{1-x}$Na$_x$AsSe$_2$. This arises from the decreased covalent character of the Na···Se interaction compared to the Li···Se interaction, which results in slightly stronger As−Se bonds.

In addition to the three short covalent As−Se bonds in the $(1/\infty)[AsSe_2^-]$ chains, there exist three long As···Se secondary interactions (Figure 1f). Such weak secondary interactions are believed to be one of the major driving forces in stabilizing the different conformations of $(1/\infty)[AsSe_2^-]$ chains with different structure-directing cations. For example, KAsSe$_2$ and RbAsSe$_2$

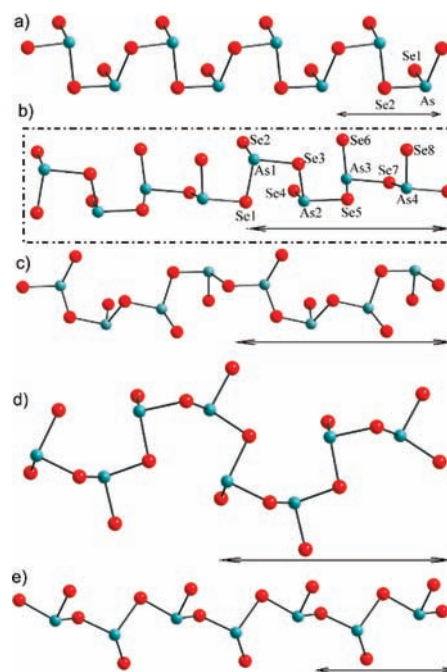(27) (a) Minceva-Sukarova, B.; Jovanovski, G.; Makreski, P.; Soptrajanov, B.; Griffith, W.; Willis, R.; Grzetic, I. *J. Mol. Struct.* **2003**, *651*, 181–189. (b) Wu, Y. D.; Bensch, W. *Inorg. Chem.* **2009**, *48*, 2729–2731.
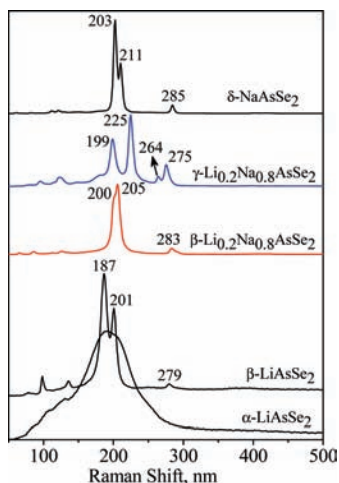
**Figure 2.** Various conformers of the single $(1/\infty)[AsSe_2^-]$ chain derived from the corner-sharing AsSe$_3$ pyramids: (a) the *zweier* chain in β-LiAsSe$_2$ (**II**) and δ-NaAsSe$_2$ (**IV**); (b) the new *vierer* single chain in γ-NaAsSe$_2$ (**III**) and γ-Na$_{0.8}$Li$_{0.2}$AsSe$_2$ (**IIIa**); (c, d) the known *vierer* single chain in (c) KAsQ$_2$[13b] and (d) RbAsQ$_2$;[13b] (e) the *zweier* single chain in CsAsQ$_2$. Parts c−e are reproduced from the published structures.[13b]

exhibit *vierer* (Figure 2c,d) and CsAsSe$_2$ exhibits *zweier* single chains (Figure 2e). One As···Se secondary interaction is within the chain (intrachain), and two others are with the neighboring chains (interchain). When these contacts are taken into account, largely distorted octahedral coordination spheres can be assigned to the As$^{3+}$ atoms (Figure 1f).

The size of the As atom is prone to having a distorted coordination environment in chalcoarsenates. The heavier

**Figure 3.** Raman spectra of **I**, **II**, **IIa**, **IIIa**, and **IV**. Three different structural phase transitions ($\alpha-\beta$, $\beta-\gamma$, and $\gamma-\delta$) are clearly evident from the change in the Raman spectra.

**Table 3.** Selected Bond Distances (Å) and Angles (deg) for $\gamma$-NaAsSe$_2$ at 100 K with Standard Deviations in Parentheses

| As(1)−Se(8) | 2.343(3) | Na(1)−Se(1) | 2.990(9) |
|---|---|---|---|
| As(1)−Se(5) | 2.453(2) | Na(1)−Se(7) | 2.948(8) |
| As(1)−Se(1) | 2.514(3) | Na(1)−Se(8) | 2.959(9) |
| As(2)−Se(7) | 2.325(3) | Na(1)−Se(2) | 2.896(9) |
| As(2)−Se(1) | 2.440(3) | Na(1)−Se(7) | 2.977(8) |
| As(2)−Se(6) | 2.475(3) | Na(1)−Se(1) | 2.986(9) |
| As(3)−Se(2) | 2.339(3) | Na(2)−Se(4) | 2.960(9) |
| As(3)−Se(6) | 2.459(3) | Na(2)−Se(2) | 2.962(9) |
| As(3)−Se(3) | 2.516(3) | Na(2)−Se(6) | 2.965(8) |
| As(4)−Se(4) | 2.321(3) | Na(2)−Se(2) | 2.968(9) |
| As(4)−Se(3) | 2.440(3) | Na(2)−Se(6) | 3.012(8) |
| As(4)−Se(5) | 2.475(3) | Na(2)−Se(1) | 3.287(9) |
| | | | |
| Se(8)−As(1)−Se(5) | 101.05(10) | Na(3)−Se(3) | 3.013(8) |
| Se(8)−As(1)−Se(1) | 101.99(10) | Na(3)−Se(2) | 2.948(9) |
| Se(5)−As(1)−Se(1) | 94.49(10) | Na(3)−Se(8) | 2.957(9) |
| Se(7)−As(2)−Se(1) | 103.50(11) | Na(3)−Se(4) | 2.960(8) |
| Se(7)−As(2)−Se(6) | 99.14(11) | Na(3)−Se(4) | 2.961(8) |
| Se(1)−As(2)−Se(6) | 97.34(9) | Na(3)−Se(3) | 3.010(8) |
| Se(2)−As(3)−Se(6) | 101.37(10) | Na(4)−Se(7) | 2.917(9) |
| Se(2)−As(3)−Se(3) | 102.13(10) | Na(4)−Se(8) | 2.950(8) |
| Se(6)−As(3)−Se(3) | 93.63(10) | Na(4)−Se(5) | 2.967(9) |
| Se(4)−As(4)−Se(3) | 102.86(10) | Na(4)−Se(8) | 2.993(8) |
| Se(4)−As(4)−Se(5) | 100.17(10) | Na(4)−Se(5) | 3.021(9) |
| Se(3)−As(4)−Se(5) | 96.08(10) | Na(4)−Se(3) | 3.329(9) |

congeners, Sb and Bi, extend their coordination number beyond 3 in most cases and form a wide variety of structure types with dimensionalities of 1−3.[11,28] Compounds of Sb and Bi with the same stoichiometry as the title compounds, i.e. AMQ$_2$, have less distorted or even regular polyhedra: e.g., NaSbSe$_2$, NaSbTe$_2$, LiSbTe$_2$, LiBiS$_2$, KBiS$_2$, RbBiS$_2$, $\alpha$-CsBiS$_2$, KBiSe$_2$, and RbBiSe$_2$[29] all adopt the NaCl structure.[13a,30] The cubic structure, however, may be an artifact (see PDF discussion below). When it comes to the As analogues, the NaCl structure type of $\delta$-NaAsSe$_2$ is stable only at high pressure (37 kbar, 600 C).[13a] As we described above LiAsSe$_2$ ($\alpha$ phase, **I**) can be stabilized in the NaCl structure type at ambient temperature and pressure by quenching from the molten state (see section 2.2.1). That the $\alpha$-LiAsSe$_2$ phase is a high-pressure phase is also evident in its much higher density with respect to the $\beta$ form (see Table 1).

**3.1.3. Structure of $\gamma$-NaAsSe$_2$ (III).** This compound crystallizes in the noncentrosymmetric space group $Pc$. The structure consists of densely packed parallel $(1/\infty)[\text{AsSe}_2^-]$ polymeric anionic chains and alkali-metal ions (Figure 1c). The conformation of the $(1/\infty)[\text{AsSe}_2^-]$ chain is different from that of $\beta$- and $\delta$-polymorphs and is reported here for the first time. This new *vierer* single chain (see Figure 2b) conformation preserves the noncentrosymmetric structure with higher Na substitution in the Li$_{1-x}$Na$_x$AsSe$_2$ system in comparison to the Li$_{1-x}$Na$_x$AsS$_2$

(28) (a) Iordanidis, L.; Brazis, P. W.; Kyratsi, T.; Ireland, J.; Lane, M.; Kannewurf, C. R.; Chen, W.; Dyck, J. S.; Uher, C.; Ghelani, N. A.; Hogan, T.; Kanatzidis, M. G. *Chem. Mater.* **2001**, *13*, 622–633. (b) Chung, D. Y.; Hogan, T. P.; Rocci-Lane, M.; Brazis, P.; Ireland, J. R.; Kannewurf, C. R.; Bastea, M.; Uher, C.; Kanatzidis, M. G. *J. Am. Chem. Soc.* **2004**, *126*, 6414–6428. (c) Kyratsi, T.; Chung, D. Y.; Ireland, J. R.; Kannewurf, C. R.; Kanatzidis, M. G. *Chem. Mater.* **2003**, *15*, 3035–3040. (d) McCarthy, T. J.; Tanzer, T. A.; Kanatzidis, M. G. *J. Am. Chem. Soc.* **1995**, *117*, 1294–1301. (e) Iordanidis, L.; Kanatzidis, M. G. *Angew. Chem., Int. Ed.* **2000**, *39*, 1928. (f) Kim, J.-H.; Chung, D.-Y.; Kanatzidis, M. G. *Chem. Commun.* **2006**, *15*, 1628–1630. (g) Chung, D. Y.; Choi, K. S.; Iordanidis, L.; Schindler, J. L.; Brazis, P. W.; Kannewurf, C. R.; Chen, B. X.; Hu, S. Q.; Uher, C.; Kanatzidis, M. G. *Chem. Mater.* **1997**, *9*, 3060–3071. (h) McCarthy, T. J.; Kanatzidis, M. G. *Chem. Mater.* **1993**, *5*, 1061–1063. (i) Chondroudis, K.; McCarthy, T. J.; Kanatzidis, M. G. *Inorg. Chem.* **1996**, *35*, 840–844.
(29) (a) Voroshilov, Y. V.; Peresh, E. Y.; Golovei, M. I. *Inorg. Mater.* **1972**, *8*, 677. (b) Bazakutsa, V. A.; Lazarev, V. B.; Gnidash, N. I.; Podyachaya, E. N.; Trippel, A. F. *Inorg. Mater.* **1986**, *22*, 1098–1101.
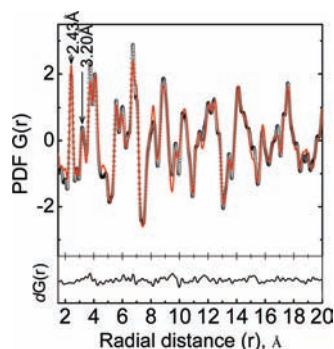(30) Gattow, G.; Zemann, J. Z. *Anorg. Allg. Chem.* **1955**, *279*, 324–327.

system, where we were able to substitute only 40% Na with preservation of the noncentrosymmetric structure.[15] Selected bond distances and angles are given in Table 3.

The importance of being able to include more Na in the noncentrosymmetric structure will be discussed in section 3.5. $\gamma$-NaAsSe$_2$ provides a rare example where a conformational change of the building units leads to the stabilization of a polar structure. The *vierer* single chain in this compound (Figure 2b) is different from the *vierer* single chain in KAsSe$_2$ or RbAsSe$_2$ (see Figure 2c,d). The rotational flexibility of the individual AsSe$_3$ pyramid within the chain is responsible for the stabilization of the different conformers and may also allow for other conformers with different counterions. Variation of the synthetic conditions as well as the structure-directing agents could lead to stabilization of new chain conformers with intriguing structures and properties.

The packing of the 1-D chains is shown in Figure 1c,d, and the noncentrosymmetric motif is clear from Figure 1c. The alkali-metal ions are in a distorted-octahedral environment of Se atoms. The edge sharing and corner sharing of the NaSe$_6$ octahedra give rise to a densely packed three-dimensional structure, which is different from the LiSe$_6$ packing in $\beta$-LiAsSe$_2$ (see the Supporting Information).

**3.1.4. Pair Distribution Function (PDF) Analysis of $\alpha$-LiAsSe$_2$ and $\beta$-LiAsSe$_2$.** The perfect octahedral coordination geometry of the As$^{3+}$ atoms in cubic $\alpha$-LiAsSe$_2$ (suggested by the single-crystal structure refinement) was unexpected and surprising. Because of the strong tendency of the lone pair of electrons in As$^{3+}$ to be stereochemically expressed (as observed in the other structural forms reported here), we examined the local structure of As$^{3+}$ in detail using PDF.

The advantage of the PDF method over crystallographic methods, such as Rietveld and typical single-crystal diffraction analysis, is the elaboration of both Bragg and diffuse intensity (total scattering) into the crystal structure modeling. Thus, the PDF technique can provide information about the local and long-range arrangement of atoms, regardless of the degree of ordering. Because of this, the technique can easily detect structural

**Figure 4.** Pair distribution function $G(r)$ plot of the monoclinic $\beta$-LiAsSe$_2$ (**II**) at 100 K. The crystallographic model (red solid line) fits the experimental data (open circles) very well, indicating the correctness of the single-crystal structure. The difference curve of $G(r)$ of the model from the experimental data is shown at the bottom.
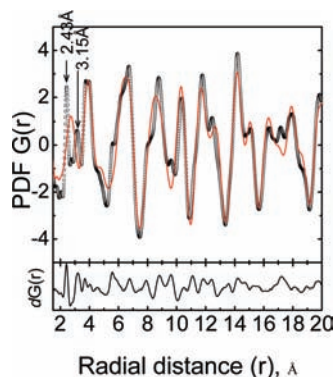


**Figure 5.** Pair distribution function plot of the cubic $\alpha$-LiAsSe$_2$ (**I**) model at 100 K. The disagreement of the cubic model (red solid line) with the experimental data (open circles) is apparent especially in the low-$r$ region (short range), where the peaks at 2.43 and 3.15 Å are not present in the model. The difference curve of $G(r)$ of the model from the experimental data is shown at the bottom.

artifacts arising from structure averaging that result from conventional crystallography.

First, we performed a PDF study on the monoclinic $\beta$-LiAsSe$_2$ phase to check the validity of its single-crystal structure refinement. The experimental PDF plot (open circles) is shown in Figure 4 together with the fit (red solid line) of the single-crystal model obtained for $\beta$-LiAsSe$_2$. The agreement between the model and experimental data is very good, since the single-crystal structure can account successfully for all the observed peaks. The small differences between the model and experimental data are attributed to the light Li atoms and their relatively small atomic X-ray scattering factor. The small scattering contribution results in a weak contribution to the PDF. This is complicated by the fact that the Li–Se and As–Se vectors overlap significantly.

The experimental PDF plot of $\alpha$-LiAsSe$_2$ is shown in Figure 5. The peak positions at low $r$ range (<5 Å) are similar to those found in $\beta$-LiAsSe$_2$ (Figure 4). In the range above 5 Å there are fewer peaks in the case of $\alpha$-LiAsSe$_2$, indicating a relatively simpler structure, which is consistent with an average NaCl structure. Interestingly, the cubic model ($Fm\bar{3}m$: one site with mixed 50% occupancy between Li and As and another site with Se) fails to describe all the features of the experimental PDF ($R \approx 37\%$).[20c] The disagreement is apparent in the low $r$ region of the PDF, where an average peak at $\sim$2.7 Å in the model (scaling factor and cell parameters were refined against the
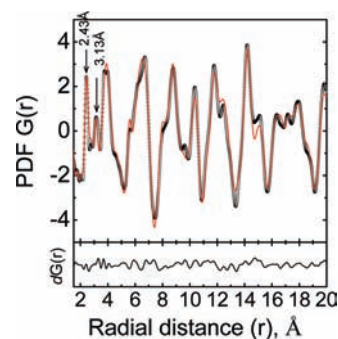


**Figure 6.** Pair distribution function plot of the proposed model (see text) for $\alpha$-LiAsSe$_2$ (**I**) at 100 K. The model is in very good agreement with the experimental data. The difference curve of $G(r)$ is shown at the bottom.

**Table 4.** Crystal System, Cell Parameters, Atomic Fractional Coordinates, and Isotropic Thermal Factors of $\alpha$-LiAsSe$_2$ Obtained after the PDF Fit[31]

| space group | $P\bar{1}$ |
|---|---|
| cryst syst | triclinic |
| cell params | |
| $a$, Å | 5.550 |
| $b$, Å | 5.580 |
| $c$, Å | 5.577 |
| $\alpha$, deg | 92.7 |
| $\beta$, deg | 90.8 |
| $\gamma$, deg | 91.5 |

| label | $x$ | $y$ | $z$ | $U_{iso}$ |
|---|---|---|---|---|
| Li | 0.2805 | 0.7182 | 0.0550 | 0.020 |
| As | 0.1953 | 0.2503 | 0.4624 | 0.030 |
| Se1 | 0.2405 | 0.7300 | 0.5050 | 0.019 |
| Se2 | 0.2559 | 0.2695 | 0.0325 | 0.046 |

experimental data) is absent in the experimental PDF, which contains two peaks located at $\sim$2.4 and $\sim$3.0 Å. This suggests that the cubic NaCl-type model is incorrect and is a consequence of unit cell averaging, derived from the single-crystal refinement. The local structure is in fact similar to that found in $\beta$-LiAsSe$_2$ but with a different long-range ordering, as indicated by large differences in the high-$r$ regions (Figures 4 and 5).

To elucidate the local structure of $\alpha$-LiAsSe$_2$ using the PDF data, we constructed a triclinic cell with the same cell parameters as that of the cubic cell. A starting model containing the smallest repeating fragment of the $(1/\infty)[\text{AsSe}_2^-]$ chain and one Li atom was constructed. This structural model was fit against the experimental data without constraints ($P1$) and yielded an excellent fit ($R \approx 18\%$) (Figure 6). A center of symmetry was found after inspection of the refined coordinates, and a $P\bar{1}$ space group was used for the final refinement (the agreement factor remained practically unchanged with almost half the number of refined parameters) (Table 4). The structure is shown in Figure 7a and consists of cyclic $[\text{As}_2\text{Se}_4]^{2-}$ units connected by Li atoms, resulting in one-dimensional LiAsSe$_2$ chains running along the diagonal of the $ac$ plane of the cubic cell (Figure 7b). Each cyclic $[\text{As}_2\text{Se}_4]^{2-}$ unit is composed of two pyramidal AsSe$_3$ centers that share two Se atoms on a distorted square plane. The two As–Se distances in the plane are 2.43 and 2.68 Å.[31]

(31) The propagation of the uncertainties from the raw data (reduction with PDFGetX) to the refined parameters (PDFfit2) is not estimated correctly; therefore, no estimated standard deviations are reported for the refined parameters. Instead, the values were truncated to the number of reported significant figures.
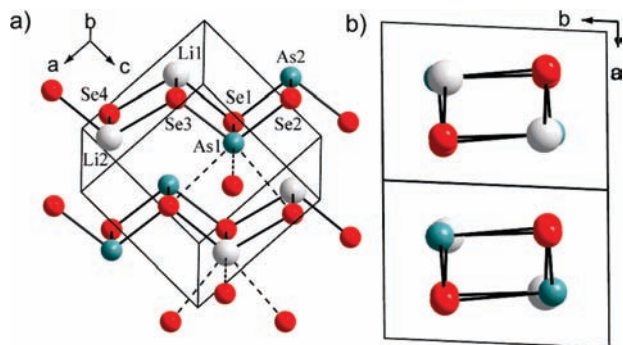
**Figure 7.** Distorted structure of α-LiAsSe$_2$ obtained by PDF analysis: (a) connectivity between [As$_2$Se$_4$]$^{2-}$ units with Li$^+$, with relatively long As−Se (>2.941 Å) and Li−Se (>3.013 Å) bonds represented by dotted lines; (b) different view showing the packing of 1D chain built of [As$_2$Se$_4$]$^{2-}$ units connected to Li$^+$. Longer As−Se and Li−Se contacts are removed for clarity.

The third Se atom is located above and below the plane at a distance of 2.43 Å and an angle of ∼98°. A similar geometry is adopted by the Li atoms that also form pyramidal LiSe$_3$ units. The Li−Se distances in the plane are 2.50 and 2.62 Å, and those above and below the plane are 2.52 Å and are at an angle of ∼103°. The coordination environments around As and Li atoms are similar; therefore, an occupational disorder could be possible. The above results underscore the strong tendency of AMQ$_2$-type compounds (where A = alkali metal, Ag; M = As, Sb, Bi; Q = S, Se, Te) to undergo local distortions that pyramidalize the M elements. Therefore, the members of AMQ$_2$ that have been reported previously as NaCl type need to be re-examined using PDF analysis.

**3.2. Synthesis, Characterization, and Polymorphic Transitions.** The syntheses of the alkali-metal selenoarsenates were achieved in quantitative yield with intermediate-temperature solid-state fusion reactions using stoichiometric mixtures of Li$_2$Se, Na$_2$Se, As, and Se at 500 °C. The temperature cooling profile was found to have a key influence on the reaction outcome. Figure 8 summarizes the various polymorphs obtained from different synthesis procedures at different compositions. The compounds are stable under ambient conditions for up to 4 weeks.

Pure β-LiAsSe$_2$ (**II**) and its Na-substituted analogues β-Li$_{1-x}$Na$_x$AsSe$_2$ in the composition range 0 < x ≤ 0.5 can be synthesized by both slow cooling of the melt and flame melt-quenching reactions. The β-LiAsSe$_2$ phase was mentioned previously, but to the best of our knowledge a structural characterization has not been reported.[14b]

Differential thermal analysis (DTA) of the as-prepared β-Li$_{1-x}$Na$_x$AsSe$_2$ (0 < x ≤ 0.5) samples showed single melting and crystallization events (see Figure 9b). However, β-LiAsSe$_2$ (x = 0) showed two endothermic events (at 455 and 523 °C) and two exothermic events (at 416 and 515 °C) (see Figure 9a). The possibility of incongruent melting of **II** was ruled out by confirming the full recovery (as judged by powder X-ray diffraction, UV−vis diffuse reflectance spectroscopy, Raman spectroscopy) of the compound after cooling of the melt. This suggested that the 455 °C endotherm is due to a phase transition, while that at 523 °C arises from the melting point. Thus, the existence of a metastable phase at high temperature (455 °C) was explored.

This was done by quenching the melt from >500 °C in water and resulted in the metastable α-LiAsSe$_2$ (**I**). Though α-LiAsSe$_2$ is stable under ambient conditions, it transforms to the more

stable β-LiAsSe$_2$ upon annealing at 400 °C for ∼2 h. In Li$_{1-x}$Na$_x$AsSe$_2$, the α phase is stable only in a very narrow composition range, 0 ≤ x < 0.1, suggestive of the fact that the lighter Li atom, which can move more easily within the framework at high temperature, is crucial in stabilizing the metastable NaCl-type phase and that can be suppressed by doping the Li site with heavier atoms such as Na.

Further increase of the Na fraction in Li$_{1-x}$Na$_x$AsSe$_2$ above 0.5 leads to the appearance of the γ polymorph, which is always observed as a byproduct of the slow-cooled synthesis of the β phase (Figure 8). Pure β polymorph in the composition range of 0.5 < x ≤ 0.8 was only achieved by quenching a stoichiometric mixture of "Li$_{1-x}$Na$_x$AsSe$_2$" sample from above 600 °C in cold water (Figure 8). Powder X-ray diffraction showed a shifting of Bragg peaks to lower 2θ angles compared to the simulated pattern of β-LiAsSe$_2$ (**II**), in accord with substitution of Na$^+$ ions in place of the smaller Li$^+$ ions (see the Supporting Information). Other spectroscopic techniques, such as Raman scattering and energy band gap measurements, are also consistent with the presence of the pure β phase (Figure 3).

The phase-pure γ polymorph can only be formed at the composition x = 0.8. γ-Li$_{0.2}$Na$_{0.8}$AsSe$_2$ (**IIIa**) can be synthesized by three different techniques: (i) by annealing β-Li$_{0.2}$Na$_{0.8}$AsSe$_2$ (**IIa**) at 400 °C, (ii) by slowly cooling **IIa** from 500 °C, and (iii) by slowly cooling the stoichiometric mixtures of Li$_2$Se/Na$_2$Se/As/Se from 500 °C (cf. section 2.2.3). The above results confirm the interconvertibility of β and γ phases at x = 0.8 and also prove that the latter is the thermodynamically stable phase. The β and γ phases crystallize in the polar monoclinic space groups Cc and Pc, respectively, with two different (1/∞)[AsSe$_2^-$] polymeric anionic chain conformations (cf. section 3.1.4). The polar structures of **IIa** and **IIIa** enable the comparative investigation of second harmonic generation (SHG) responses (section 3.5). The powder X-ray diffraction study after DTA of β-Li$_{0.2}$Na$_{0.8}$AsSe$_2$ confirms that it transforms to the γ polymorph with a 10 °C heating/cooling rate and it shows one melting and one crystallization point (Figure 9b). We did not observe any thermal characteristics in the DTA corresponding to the polymorphic transitions, which could show up as an exothermic event in the thermal analysis experiments: e.g., CsBiS$_2$ (β and γ forms).[32] This may be because of the small energy difference between the β and γ phases.

The fully Na substituted phase in the Li$_{1-x}$Na$_x$AsSe$_2$ system (i.e., x = 1) was found to adopt two structural forms. The synthesis and structure of one (referred to as δ-NaAsSe$_2$) has been reported previously.[13a] We discovered the new polymorph of NaAsSe$_2$ (referred to as γ-NaAsSe$_2$) by intermediate-temperature solid-state fusion reactions (Figure 8). Similar to the synthesis of γ-Li$_{0.2}$Na$_{0.8}$AsSe$_2$ (**IIIa**), γ-NaAsSe$_2$ (**III**) can also be synthesized using three different techniques: (i) annealing of δ-NaAsSe$_2$ (**IV**) at 400 °C, (ii) slow cooling of **IV** from 500 °C, and (iii) slow cooling of stoichiometric mixtures of Na$_2$Se/As/Se from 500 °C. Therefore, the γ and δ polymorphs are interconvertible and the former is the thermodynamically stable phase. The powder X-ray diffraction study after DTA confirms the clean conversion of the γ to the δ phase with a 10 °C/min heating/cooling rate. Similar to the DTA behavior of β-Li$_{0.2}$Na$_{0.8}$AsSe$_2$, here too we could not observe any thermal characteristics corresponding to the polymorphic transitions. This may be due to the small energy difference between the γ and δ phases.
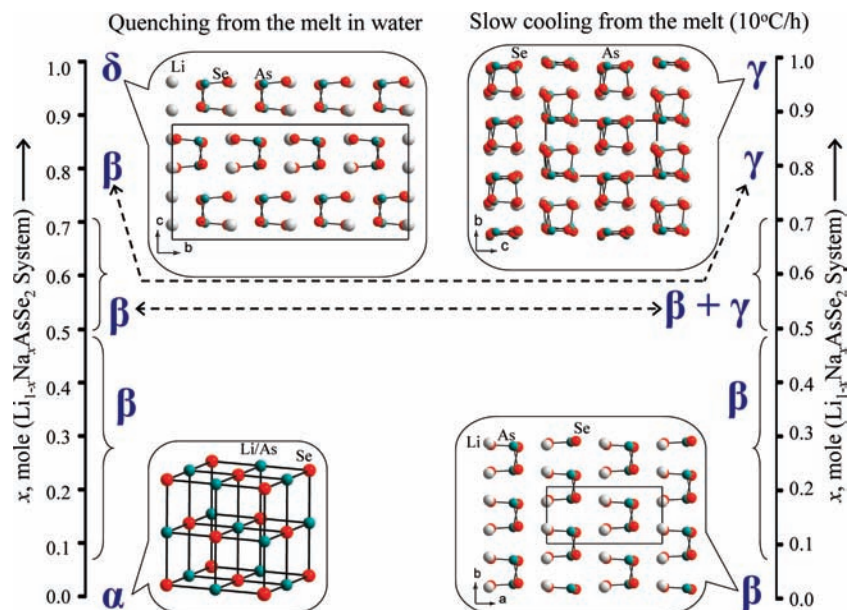
**Figure 8.** Composition/structure diagram of the four different structure varieties (polymorphs) in the $Li_{1-x}Na_xAsSe_2$ system. At $x = 0$, the $\alpha$ phase is obtained by quenching the melt and the $\beta$ phase is obtained by slowly cooling the melt. At the $0.1 \leq x \leq 0.5$ range only the $\beta$ phase is observed, whereas at the $0.5 < x \leq 0.7$ composition range both $\beta$ and $\gamma$ phases appear. Pure $\beta$ phase in the $0.5 < x \leq 0.7$ range is obtained by melt quenching. At $x = 0.8$, $\beta$ phase is obtained by melt quenching and the $\gamma$ phase is obtained by slowly cooling the melt. At $x = 1$, the $\delta$ phase is obtained by melt quenching and the $\gamma$-phase by slowly cooling the melt.



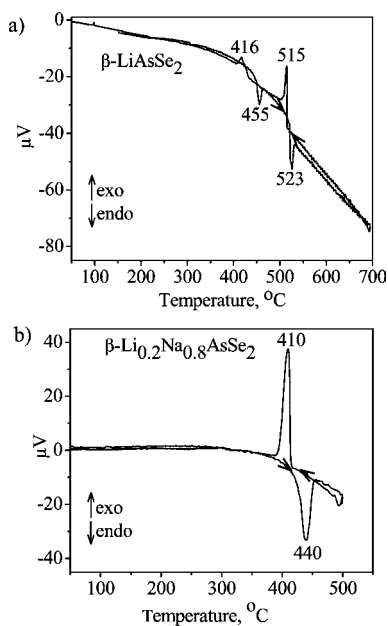**Figure 9.** Differential thermal analysis (DTA) of (a) $\beta$-$LiAsSe_2$, showing two melting (endothermic) and two crystallization (exothermic) points, and (b) $\beta$-$Li_{0.2}Na_{0.8}AsSe_2$. The $y$ axis represents heat flow.

The solubility of $AAsQ_2$ was tested in common solvents in order to explore their future potential for solution processing of thin films.[33] All compounds were found to be completely soluble in anhydrous hydrazine without decomposition (tested

by the solution recovery of the materials) and produced yellow and red solutions of $AAsS_2$ and $AAsSe_2$, respectively (see the Supporting Information). Dissolution in methanol is also possible by using a few drops of hydrazine followed by an excess of methanol.[34]

**3.3. UV−Visible−Near-IR Spectroscopy.** The optical absorption properties of $\alpha$-$LiAsSe_2$, $\beta$-$LiAsSe_2$, $\gamma$-$Li_{0.2}Na_{0.8}AsSe_2$, $\gamma$-$NaAsSe_2$, and $\delta$-$NaAsSe_2$ were investigated with UV−visible−near-IR diffuse reflectance spectroscopy. The compounds show steep absorption edges corresponding to energy band gaps of $1.11-1.75$ eV, depending on the structure type and composition (see Figure 10 and Table 5). The sharp vertical absorption edge is suggestive of direct band gap nature, which is supported by the first-principles electronic band structure calculations to be described below. The variation of band gap with composition, $x$, is shown in Figure 10d, which correlates very well with the unit cell volume vs $x$ plot (Figure 11).

From Figure 10d, it is clear that there is a negligible difference in the band gap between $\alpha$ and $\beta$ forms of $LiAsSe_2$, whereas the band gap difference between the $\beta$ and $\gamma$ forms (Figure 10b) as well as between the $\gamma$ and $\delta$ forms (Figure 10c) is clearly evident. Although the $\gamma$ phase is more dense than both the $\beta$ and $\delta$ phases, it is surprising that a reverse band gap order is observed, namely $E_g(\gamma$-$NaAsSe_2) > E_g(\delta$-$NaAsSe_2)$. The increase of the band gap of $Li_{1-x}Na_xAsSe_2$ with increasing Na fraction is consistent with the substitution of Li by the more electropositive Na. Similar to the case for $LiAsS_2$, in which an unusual optical band gap trend was observed (i.e., $E_g(LiAsS_2) < E_g(As_2S_3)$), here also we found narrower band gaps for $\alpha$- and $\beta$-$LiAsSe_2$ in comparison to $As_2Se_3$ ($E_g = 1.85$ eV)[35] (Figure 10a).

In the $LiAsS_2$ system, we have shown by both theoretical and experimental techniques that weak interchain interactions play a major role in bandwidth formation and result in lowering

(32) McCarthy, T. J.; Ngeyi, S. P.; Liao, J. H.; Degroot, D. C.; Hogan, T.; Kannewurf, C. R.; Kanatzidis, M. G. *Chem. Mater.* **1993**, *5*, 331–340.
(33) (a) Mitzi, D. B.; Kosbar, L. L.; Murray, C. E.; Copel, M.; Afzali, A. *Nature* **2004**, *428*, 299–303. (b) Mitzi, D. B. *Adv. Mater.* **2009**, *21*, 3141–3158.
(34) Bera, T. K.; Kanatzidis, M. G. Manuscript in preparation, 2009.

(35) Stergiou, A. C.; Rentzeperis, P. J. *Z. Kristallogr.* **1985**, *173*, 185–191.
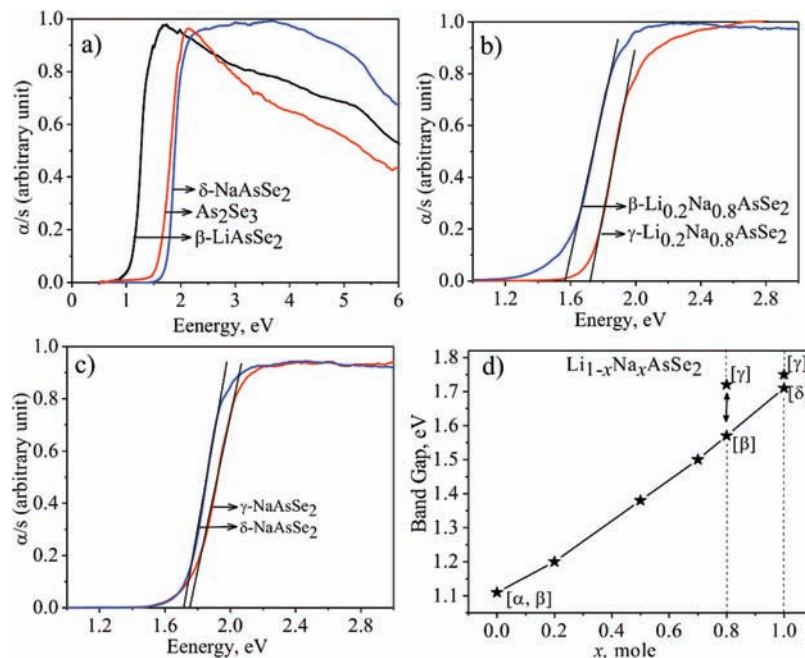
**Figure 10.** (a) Solid-state UV−vis optical absorption spectra of **II**, **IV**, and As$_2$Se$_3$. (b) Comparison of the band-edge absorptions between **IIa** and **IIIa**. (c) Band-edge absorption comparison between **III** and **IV**. (d) Band-gap evolution with composition in Li$_{1-x}$Na$_x$AsSe$_2$.

**Table 5.** AAsQ$_2$ Materials: Summary

| direct-band-gap material | space group | center of symmetry | $(1/\infty)$[AsQ$_2^-$] chain conformation | rel SHG intensity[a] | band gap[b](eV) | melting point (°C) | crystallizn point (°C) |
|---|---|---|---|---|---|---|---|
| LiAsS$_2$ | $Cc$ | no | Figure 2a | ~10 | 1.60 | 524 | 503 |
| Li$_{0.6}$Na$_{0.4}$AsS$_2$ | $Cc$ | no | Figure 2a | ~30 | 1.88 | 480 | 460 |
| Li$_{0.5}$Na$_{0.5}$AsS$_2$ | $Pbca$ | yes | Figure 2a | n/a | 2.07 | 470 | 450 |
| NaAsS$_2$ | $P2_1/b$ | yes | Figure 2a | n/a | 2.33 | 515 | 460 |
| $\alpha$-LiAsSe$_2$ | $Fm\overline{3}m$ | yes | n/a | n/a | 1.10 | 455 | 416 |
| $\beta$-LiAsSe$_2$ | $Cc$ | no | Figure 2a | n/a[c] | 1.11 | 523 | 515 |
| $\beta$-Li$_{0.2}$Na$_{0.8}$AsSe$_2$ | $Cc$ | no | Figure 2a | ~55 | 1.57 | 440 | 410 |
| $\gamma$-Li$_{0.2}$Na$_{0.8}$AsSe$_2$ | $Pc$ | no | Figure 2b | ~65 | 1.72 | 440 | 410 |
| $\gamma$-NaAsSe$_2$ | $Pc$ | no | Figure 2b | ~75 | 1.75 | 435 | 413 |
| $\delta$-NaAsSe$_2$ | $Pbca$ | yes | Figure 2a | n/a | 1.71 | 435 | 413 |

[a] Relative to AgGaSe$_2$, measured at $\lambda$ 800 nm using powder samples (average particle size of 54($\pm$9) $\mu$m). [b] Measured by diffuse reflectance spectroscopy using powder samples. [c] SHG data are not available because of the experimental limitations.



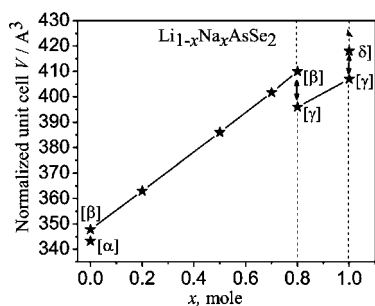**Figure 11.** Plot of the normalized unit cell volume vs composition in the Li$_x$Na$_{1-x}$AsSe$_2$ system. Three distinct structural phase transitions are clearly evident from the plot.

of the band gaps of the ternaries relative to that of the parent compound As$_2$S$_3$.[12a,15] The AAsQ$_2$ (A = Li, Na; Q = S, Se) chalcoarsenates are high-absorbing, direct-band-gap semiconductors and could be promising as light-harvesting components in solar cells, because their optical absorption lies within the range of the solar spectrum.[36] The band-gap tunability by proper stoichiometric substitution of Li by Na in Li$_{1-x}$Na$_x$AsQ$_2$ is an additional advantage in fabricating monolithically interconnected heterojunction tandem solar cells where the narrow-band-gap $\beta$-LiAsSe$_2$ ($E_g$ = 1.11 eV) can be used in the bottom part of

the cell and the wide-band-gap NaAsS$_2$ ($E_g$ = 2.23 eV) in the top.[37] This could result in harvesting almost the entire solar spectrum.

**3.4. Band Structure and Total Energy Calculations.** In order to better understand the electronic structures of these materials, we performed first-principles electronic band structure calculations for the ground and excited states using the highly precise full-potential linearized augmented plane wave (FLAPW)[13a] method with the screened-exchange local density approximation (sX-LDA)[23b] as well as the Hedin−Lundqvist form of the exchange-correlation potential (LDA).[23c] To the best of our knowledge, these are the first theoretical calculations performed on this class of materials. The calculations show that the band gap of $\gamma$-NaAsSe$_2$ (**III**) is almost direct while that of $\delta$-NaAsSe$_2$ (**IV**) is direct at the $\Gamma$ point (Figure 12a,b). For $\gamma$-NaAsSe$_2$, the valence band maximum (VBM) occurs at D

(36) Markvart, T.; Castaner, L., *Solar Cells: Mateials, Manufacture, and Operation*; Elsevier: Amsterdam, 2005.

(37) (a) Geisz, J. F.; Kurtz, S.; Wanlass, M. W.; Ward, J. S.; Duda, A.; Friedman, D. J.; Olson, J. M.; McMahon, W. E.; Moriarty, T. E.; Kiehl, J. T. *Appl. Phys. Lett.* **2007**, *91*, 023502. (b) AbuShama, J.; Noufi, R.; Johnston, S.; Ward, S.; Wu, X. *Conf. Rec. IEEE Photovoltaic Spec. Conf.* **2005**, 299–302. (c) Green, M. A.; Emery, K.; Hishikawa, Y.; Warta, W. *Prog. Photovoltaics* **2008**, *16*, 435–440.
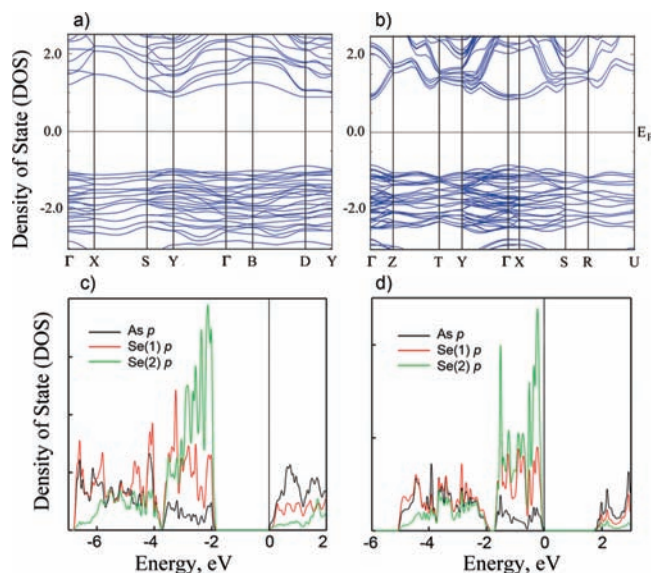
**Figure 12.** Calculated band structures of (a) $\gamma$-NaAsSe$_2$ and (b) $\delta$-NaAsSe$_2$. (c) Projection of the electronic density of states (DOS) of $\gamma$-NaAsSe$_2$ for individual elements (As and Se). (d) DOS of $\delta$-NaAsSe$_2$. Se(1) and Se(2) are the bridging and terminal atoms respectively.

**Table 6.** Calculated Total Energy (hartree) and Band Gaps (eV) for $\gamma$-NaAsSe$_2$ and $\delta$-NaAsSe$_2$

|  | $\gamma$-NaAsSe$_2$ | $\delta$-NaAsSe$_2$ | diff |
|---|---|---|---|
| total energy by LDA | −7 273.801 31 | −7 273.803 44 | 0.058 |
| exptl band gap | 1.75 | 1.71 | 0.04 |
| calcd band gap | 1.77 | 1.69 | 0.08 |

while the conduction band minimum (CBM) occurs at Y, which is only 0.7 meV lower than that at D (Figure 12a). Here too the sX-LDA method with the FLAPW approach shows great improvements of the excited electronic states over the LDA method and again has yielded excellent estimates of the band gaps (see Table 6).[23b,38]

The band structures of **III** and **IV** along with the projection of the electronic density of states (DOS) for individual elements (As and Se) are shown in parts a−d of Figures 12, respectively. From the DOS plot, it is clear that the bands around the Fermi level ($E_F$) are predominantly As and Se states. A detailed analysis of the DOS reveals that these are mainly composed of As 4p and Se 4p orbitals, suggesting that the p−p mixing has a strong effect on the electronic properties of the compounds. Furthermore, the DOS in Figure 12c,d demonstrates that the bridging atom Se(1) has stronger hybridization with As than the terminal atom Se(2). Namely, the p orbital atomic environment of Se(2) occupies mainly lower energy levels (−5.0 to −2.0 eV below the valence band maximum) while that of the terminal Se(1) atom has more donated electrons from Na and contributes most to the higher energy levels (−2.0 eV to the valence band maximum) in the valence bands. The valence band edge is mainly Se 4p in nature, whereas the conduction band edge has mainly As 4p character. The fundamental band edge excitation is mostly from the Se 4p to the As 4p type orbitals. The calculated band gaps ($E_{cal}$ = 1.77 eV for $\gamma$-NaAsSe$_2$ and 1.69 eV for $\delta$-NaAsS$_2$) show very good agreement with the measured band gaps (1.75 and 1.71 eV, respectively) (Table 6).

(38) Asahi, R.; Mannstadt, W.; Freeman, A. J. *Phys. Rev. B* **1999**, *59*, 7486–7492.
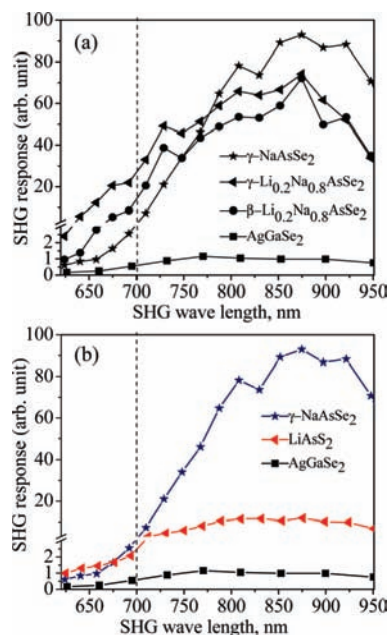
**Figure 13.** Comparison of the SHG response for (a) $\beta$-Li$_{0.2}$Na$_{0.8}$AsSe$_2$, $\gamma$-Li$_{0.2}$Na$_{0.8}$AsSe$_2$, and $\gamma$-NaAsSe$_2$ relative to AgGaSe$_2$ and (b) $\gamma$-NaAsSe$_2$ and LiAsS$_2$ relative to AgGaSe$_2$ at different SHG wavelengths, using powder samples (average particle size of 54($\pm$9) $\mu$m). The solid lines between the points are a guide to the eye. The dotted line represents the band edge (1.80 eV) for AgGaSe$_2$.

The greater thermodynamic stability of $\gamma$-NaAsSe$_2$ observed experimentally is also verified by the first-principles total-energy calculations, which were performed on $\gamma$-NaAsSe$_2$ (**III**) and $\delta$-NaAsSe$_2$ (**IV**) within the LDA. The calculated total energy difference of 58 meV, which is equivalent to $kT$ at $T$ = 400 °C, implies that **III** is 58 meV lower in total energy than **IV** and is significant enough to experimentally observe the interconversion between the two polymorphs.

In order to better understand the physical origin of the greater stability of $\gamma$- over $\delta$-NaAsSe$_2$, we also carried out total energy calculations for respective single chains of these two forms. This was done on a model system where the chains were set apart from each other by up to ~8 Å to essentially eliminate any interaction between them. The calculations showed only ~28 meV more stability of the single chain in the $\delta$ over that of the $\gamma$ form. This suggests that the greater thermodynamic stability of the $\gamma$ over $\delta$ form originates from the crystal packing of the chains and not from the different conformations of the single chains themselves.

**3.5. Nonlinear Optical Properties and Second Harmonic Generation Measurements.** The remarkably strong nonlinear optical SHG response is one of the most significant properties of $\beta$-Li$_{0.2}$Na$_{0.8}$AsSe$_2$, $\gamma$-Li$_{0.2}$Na$_{0.8}$AsSe$_2$, and $\gamma$-NaAsSe$_2$. It was measured with a modified Kurtz and Perry method over a range of wavelengths (1000−2000 nm) using a laser source. A comparison of the SHG response relative to the benchmark material AgGaSe$_2$ was also done using the same particle size ranges mainly at wavelengths >700 nm (Figure 13).

Efficiency comparisons below 700 nm are not reliable because of the band-edge absorption of AgGaSe$_2$.[2a] In the wavelength range of 700−900 nm, relative SHG efficiencies of $\beta$-Li$_{0.2}$Na$_{0.8}$AsSe$_2$, $\gamma$-Li$_{0.2}$Na$_{0.8}$AsSe$_2$, and $\gamma$-NaAsSe$_2$ were ~55, 65, and 75 times stronger than that of AgGaSe$_2$ (Figure 13). This is one of the highest SHG responses ever reported. Particle size dependent SHG measurements indicated that all three

materials are type I nonphase matchable at 790 nm. The phase matchability of NLO materials is wavelength dependent: e.g., AgGaSe$_2$ is phase matchable only in the range 3800−12 400 nm.[2a] Therefore, it is possible that these materials are phase matchable at a different wavelength range beyond the one studied here.

The highly polar structure that results from the alignment of dipoles in the structure is likely responsible for the enhanced SHG intensity of these selenoarsenates.

Although the larger SHG response of $\gamma$-NaAsSe$_2$ compared to that of $\beta$-Li$_{0.2}$Na$_{0.8}$AsSe$_2$ and $\gamma$-Li$_{0.2}$Na$_{0.8}$AsSe$_2$ can naively be attributed to substitution of the more polarizable Na atom for Li, which is also consistent with the trend observed in the Li$_{1-x}$Na$_x$AsS$_2$ system,[15] its true origin lies elsewhere. This was revealed with first-principles density functional theory calculations of the NLO properties.[39]

To understand the remarkably large SHG response of $\gamma$-NaAsSe$_2$, we carried out first-principles SHG coefficient calculations[39] using the so-called length-gauge formalism derived by Aversa and Sipe.[40] The calculated static $\chi^2$ value for $\gamma$-NaAsSe$_2$ is 324.6 pm/V, which is much larger than that of LiAsS$_2$ ($\chi^2$ = 196.3 pm/V) and AgGaSe$_2$ ($\chi^2$ = 64 pm/V).[41] To the best of our knowledge, this is the highest static SHG coefficient to date among materials with band gaps larger than 1.0 eV. The quasi-one-dimensional structure of $\gamma$-NaAsSe$_2$ results in high density of states (DOS) and consequently large spatial overlap between the optical transition states to yield a large static true $\chi^2$ value. Our previous electronic structure calculations on LiAsS$_2$ yielded greatly broadened bands arising from the strong interchain interactions from the small Li cations, which weakens the anisotropic one-dimensional characteristic. This results in significantly smaller DOS near the band gap and a much smaller $\chi^2$ value relative to $\gamma$-NaAsSe$_2$. This is an enormously valuable insight. It is not the more polarizable nature of Na$^+$ over Li$^+$ that is responsible for the higher SHG efficiency of the Na-rich systems but the decrease in dimensionality that results from the larger Na$^+$ ion. As the Na$^+$ ions substitute for Li$^+$, the (1/∞)[AsSe$_2^-$] chains are increasingly pried apart from one another and interchain interactions diminish, thereby lowering the dimensionality of the system. Thus, controlling dimensionality should be a good strategy in designing better SHG materials.[39]

## 4. Concluding Remarks

The conformational flexibility of the (1/∞)[AsQ$_2^-$] single chains and the nature of the structure directing alkali-metal ions generates an impressive structural diversity in the AAsQ$_2$ (A = alkali-metal; Q = S, Se) chalcoarsenate system. The (1/∞)[AsQ$_2^-$] single chains derived from the corner-sharing

pyramidal AsQ$_3$ units and relative orientation of one AsQ$_3$ pyramid relative to another within the chain is the origin behind the existence of different chain conformers. The difference in energy between various conformers and packing arrangements is significant enough to achieve the interconversions at intermediate temperature (∼400 °C), which result in three different polymorphic transitions in Li$_{1-x}$Na$_x$AsSe$_2$. The *zweier* single chain is very common in the AAsQ$_2$ structure, as it is present in four different structures, namely LiAsS$_2$, NaAsS$_2$, $\beta$-LiAsSe$_2$, and $\delta$-NaAsSe$_2$. Undoubtedly, there are many more (1/∞)[AsQ$_2^-$] chain conformers to be isolated by judiciously varying the counterions. We have shown with pair distribution function analysis (PDF) that cubic NaCl-type $\alpha$-LiAsSe$_2$ is in fact locally severely distorted. This result raises the need for a re-examination of the structures of other AMQ$_2$ (A = alkali metal, As; M = As, Sb, Bi) families of compounds, which previously have been reported as NaCl type.

The AAsQ$_2$ materials have remarkable optical properties. The direct band gaps found in AAsQ$_2$ can be tuned by proper substitution of the alkali metals and chalcogens to lie in the spectral range that is optimal for photovoltaic applications. In combination with their strong SHG response and direct band gap nature, these materials are also soluble in common solvents such as methanol, which makes them suitable for patterned thin film deposition for device fabrication.

The extremely strong nonlinear optical SHG response of AAsQ$_2$ species makes them very promising for future NLO investigations. The large polarity of AAsQ$_2$ chalcoarsenate materials that originates from the asymmetric pyramidal AsQ$_3$ units, the large polarizability of the selenium atoms, and the low dimensionality of the structures all couple to produce record-breaking SHG coefficients, as suggested by ab initio DFT theoretical investigations. Our investigations of these systems provide a new insight and point to a very valuable design principle for NLO materials.

**Supporting Information Available:** Figures and text giving powder X-ray patterns and experimental details and CIF files giving X-ray crystallographic data for $\alpha$-LiAsSe$_2$, $\beta$-LiAsSe$_2$, and $\gamma$-NaAsSe$_2$. This material is available free of charge via the Internet at http://pubs.acs.org.

JA9094846

(39) Song, J. H.; Freeman, A. J.; Bera, T. K.; Chung, I.; Kanatzidis, M. G. *Phys. Rev. B* **2009**, *79*, 245203.
(40) (a) Sipe, J. E.; Ghahramani, E. *Phys. Rev. B* **1993**, *48*, 11705–11722. (b) Aversa, C.; Sipe, J. E. *Phys. Rev. B* **1995**, *52*, 14636–14645.
(41) Rashkeev, S. N.; Lambrecht, W. R. L. *Phys. Rev. B* **2001**, *63*, 165212–1.